ADVANCED FUNCTIONAL MATERIALS
www.afm-journal.de

Decoupling Size and Electronic Effects in Doped $SrTiO_3$ Photocatalysts Through Surface Area–Normalized CO_2 Hydrogenation Rates

*Dikshita Bhattacharyya, Baliana Shani, Isaac Holmes-Gentle, Gerardo T Martinez, Martyn McLachlan, Nicola Seriani, and Ludmilla Steier**

This study decouples size and electronic effects in Ga- and La,Ga-doped $SrTiO_3$ photocatalysts through specific surface area (SSA) normalized CO_2 hydrogenation rates. The distinction between SSA-normalized and apparent photocatalytic activity is crucial because gas-sorption experiments reveal that Ga monodoping significantly increases the SSA of sol–gel synthesized $SrTiO_3$, but does not enhance its SSA-normalized photocatalytic activity in CO_2 photohydrogenation. In contrast, SSA-normalized photocatalytic rates for La,Ga co-doped $SrTiO_3$ approximately double, suggesting a true improvement in catalytic performance. These co-doped samples show intense, sharp photoluminescence and a mid-gap absorption feature which, using DFT calculations and oxygen annealing experiments, color centers are attributed to (*e.g.*, $Ti_{Ti}^{x} - V_O^{x} - Ti_{Ti}^{x} \leftrightarrow Ti'_{Ti} - V_O^{\cdot\cdot} - Ti'_{Ti}$). Though future studies into the identification of the active site(s) are needed to assess the true, intrinsic activity, this study highlights that SSA normalization of photocatalytic rates is helpful to disentangle key material properties that enhance the catalytic activity from mere surface area effects.

1. Introduction

Oxide UV absorbers such as TiO_2, $SrTiO_3$, and their doped analogues remain a core class of photocatalyst materials primarily due to their chemical stability and excellent conversion yields of UV photons.[1] Doping or alloying strategies have been widely employed to reduce the bandgap and utilize a broader range of the solar spectrum.[2–4] However, these strategies can also significantly impact oxygen vacancy equilibria and particle size, complicating the deconvolution of factors impacting photocatalytic activity.[5–7]

Catalytic activity is reported differently across scientific communities. In photocatalysis, where catalyst suspensions are common, activity is typically expressed as a rate per gram of catalyst, following conventions from heterogeneous thermal catalysis. In contrast, photoelectrochemical systems use current density [mA cm^{-2}] at a given overpotential, akin to electrochemical benchmarking, where the geometrical area of the electrode is the key metric. In fundamental studies of the electrochemical CO_2 reduction reaction (CO_2RR), activity is normalized to the electrochemically active surface area, as measured by the chemical double layer capacitance, Pb-underpotential measurements, and, more recently, CO displacement to approximate intrinsic catalytic activity as a turnover frequency,[8,9] as is routinely done in homogeneous catalysis. In heterogeneous photocatalysis, however, we remain far from directly quantifying the intrinsic activity of catalytic sites, especially when modified by doping or other synthetic strategies. In this work, we take a first step toward that goal by normalizing photocatalytic rates to the specific surface area (SSA) of the photocatalyst. We show that apparent activity trends can shift significantly when SSA is accounted for, enabling us to distinguish improvements arising from true electronic modification from those merely due to surface area enhancement.

For example, understanding the activity of oxygen vacancies in the reduction of CO_2 is crucial for the development of improved catalyst materials and has been gaining attention in recent literature on photocatalysts,[5,10] and perhaps even more so in the field of electrochemical CO_2 reduction.[11–13] The latter bears the

D. Bhattacharyya, M. McLachlan, L. Steier
Department of Materials
Imperial College London
London SW7 2AZ, UK
E-mail: ludmilla.steier@chem.ox.ac.uk
B. Shani, I. Holmes-Gentle, L. Steier
Department of Chemistry
University of Oxford
Oxford OX1 3QZ, UK
G. T Martinez
Department of Materials
University of Oxford
Oxford OX1 3PH, UK
N. Seriani
Abdus Salam International Center for Theoretical Physics
Trieste 34151, Italy

The ORCID identification number(s) for the author(s) of this article can be found under https://doi.org/10.1002/adfm.202511923

DOI: 10.1002/adfm.202511923

advantage of studying the half-reaction in a 3-electrode electrochemical cell, which facilitates direct correlations between activity and material properties of the catalyst loaded on the working electrode. In photocatalysis, it is not possible to study half reactions without the use of scavengers.

We recently developed an interest in CO_2 photohydrogenation reaction using H_2 as the reductant instead of water. This reaction is particularly well suited to provide insight into the technologically relevant chemistry of hydrogenation reactions – an area currently dominated by heterogeneous thermal and photothermal catalysis.[14–17] Since room-temperature gas phase semiconductor-based CO_2 photohydrogenation is a rather unexplored reaction, with our previous work reporting on it for the first time using polymer photocatalysts,[18] here, we aim to establish key material property–photocatalytic activity relationships using oxide perovskites. Taking inspiration from recent studies on Al-doped $SrTiO_3$ that showed quantum efficiencies in the water splitting reaction close to 100%,[1,19] we investigate material properties and CO_2 photohydrogenation rates of $SrTiO_3$ nanoparticle photocatalysts doped with Ga^{3+} as a suitable p-block B-site dopant with well-matched ionic radii ($r(Ti^{4+})$ = 60.5 pm, $r(Ga^{3+})$ = 62.0 pm in octahedral coordination) and La^{3+} as a suitable f-block A-site dopant with reasonably matched ionic radii ($r(Sr^{2+})$ = 144 pm, $r(La^{3+})$ = 136 pm in cuboctahedral coordination (CN 12)) maintaining Goldschmidt's tolerance factors close to 1.[20,21]

There seem to be two major viewpoints on the effect of aliovalent doping. The works mentioned above attribute the high conversion yields in Al-doped $SrTiO_3$ to changes in particle morphology, exposing different facet ratios which are suggested to drive efficient spatial separation of photogenerated charge carriers through anisotropic charge transport.[1,19] Other studies attribute the improved activity to the suppression of Ti^{3+} mid-gap recombination centers.[22–24]

This shows that more clarity around the key metrics affecting the intrinsic activity of perovskite oxide photocatalysts is needed. Hence, we choose our dopants wisely to only disturb oxygen vacancy equilibria without significantly affecting the bandgap and assess SSA-normalized photoactivity as a proxy for its intrinsic activity. Even though $SrTiO_3$ is a wide bandgap absorber with limited solar-to-fuel efficiencies, investigating CO_2 photohydrogenation reactions with $SrTiO_3$ doped with elements from the p, f, and d blocks in the periodic table will be useful to establish material property-photocatalytic activity relationships for this reaction. Ultimately, this approach can help identify the catalytically active sites, drawing parallels to advances made in electrochemical CO_2 reduction.[8,25]

2. Results and Discussion

Figure 1 summarizes our findings from photohydrogenation experiments with commercial $SrTiO_3$, Ga-doped, and La,Ga-co-doped $SrTiO_3$. In the Ga-doped samples, the Ga-dopant concentration (x = [Ga]/[B site cations]) varies between 1–7% and maintains a 1:1 ratio with La in the co-doped samples. All doped samples were synthesized via the sol–gel Pechini route with the final calcination step at 900 °C. Additional details on the synthesis conditions can be found in Section S1 (Supporting Information).

Photohydrogenation experiments were carried out in a 3:1 ratio of H_2:CO_2 under irradiation with simulated sunlight (Xenon lamp, 1 sun, AM 1.5 filter). Full experimental details and time-dependent photocatalytic data are provided in Section S2 and Figure S3 (Supporting Information). Under ambient temperatures and pressures, all samples selectively evolved CO, with the rate of CO production (as measured after 6 h of irradiation) increasing monotonically as the molar dopant concentration x increased (Figure 1a). CO, produced via the reverse water gas shift reaction $H_2 + CO_2 \rightleftharpoons CO + H_2O$, is expected to be the main product on $SrTiO_3$.[26] Often, such trends are immediately investigated with respect to defect chemistry and its impact on charge carrier lifetimes.[22] However, before investigating this correlation, we first examined CO production rates normalized by specific surface area (SSA).

SSA values were obtained from N_2 and CO_2 adsorption isotherms (see Section S2 and Figure S4, Supporting Information) and are summarized in Figure 1b. Looking at the SSAs obtained from N_2 adsorption/desorption isotherms, a nearly linear increase in surface area is observed as more Ga is incorporated in the sol–gel Pechini synthesis. The La, Ga-co-doped samples show ≈2.5x smaller SSAs compared to the mono-doped samples, and the highest Ga concentrations in the mono-doped samples reached SSAs similar to the commercial $SrTiO_3$. Because we assess CO_2 hydrogenation rates, we also collected CO_2 adsorption isotherms, which are typically carried out at room temperature and hence can shed light on the effect of dopant incorporation on CO_2 adsorption. CO_2 has been reported to interact more strongly with polar surfaces due to the higher quadrupolar moment compared to N_2, providing additional insights into surface heterogeneity and active sites (such as anion vacancies, microporosity and -OH groups).[27–32] Furthermore, oxygen vacancies have been suggested to improve CO_2 adsorption, even though no distinction between an increase in surface area and a true increase in the affinity of CO_2 to the oxygen vacancy-rich surface has been shown.[13] The CO_2 adsorption isotherms shown in Figure S4b (Supporting Information) yield BET SSAs that are ≈1/3 lower than those collected from N_2 adsorption but show an almost identical trend (Figure 1b), namely a nearly linear increase in surface area as more Ga is incorporated and ≈2.5x smaller SSAs in the co-doped samples. While we are investigating whether the large offset between the N_2 and CO_2 SSAs is due to the temperature difference in adsorption isotherms as predicted by Arrhenius, here, the focus remains on the trend in SSAs, which does not suggest a particularly strong affinity to CO_2 at room temperature in the dark (see Table S1, Supporting Information ratios of SSAs obtained from N_2 and CO_2 adsorption isotherms), as suggested for Ce-doped ZnO.[13]

When the CO production rate is normalized for either SSA (Figure 1c,d), the previously near-linear trend with dopant concentration drastically changes. Now, the Ga mono-doped samples exhibit almost identical CO production rates and are intrinsically not better photocatalysts than our commercial $SrTiO_3$ reference, in contrast to our previous hypothesis based on reports on similar materials in the water-splitting reaction.[24] On the other hand, the SSA-normalized CO_2 conversion rates of La, Ga-co-doped samples approximately double compared to the mono-doped and commercial $SrTiO_3$, which seems to be linked to intrinsic differences between the mono-doped and co-doped materials,

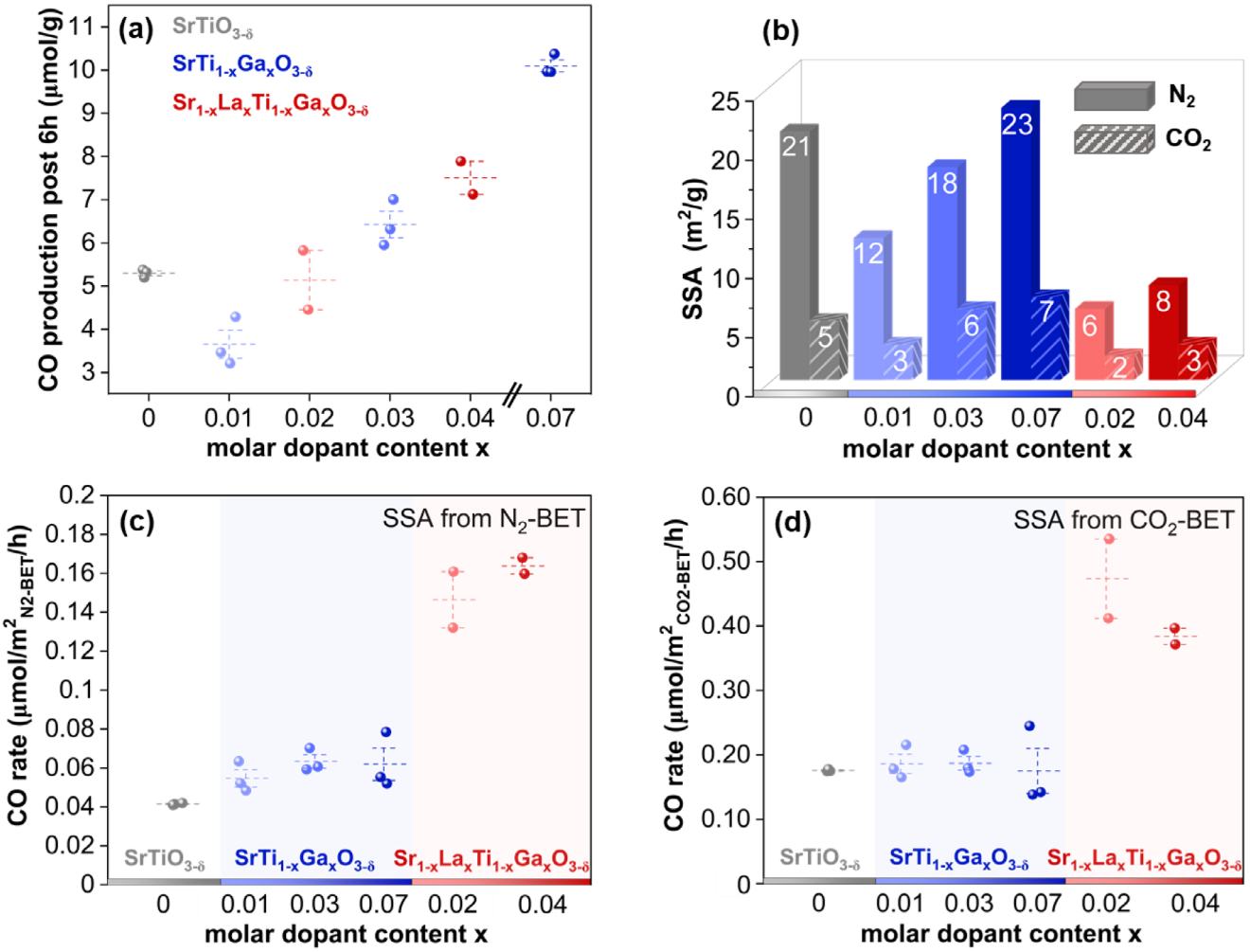

Figure 1. CO_2 photohydrogenation with commercial $SrTiO_3$ (grey), Ga-doped (blue), and La, Ga-co-doped $SrTiO_3$ (red). a) Carbon monoxide (CO) evolution expressed in micromoles of CO produced per gram of catalyst after a reaction time of $t = 6$ h. b) Specific surface area (SSA in m^2g^{-1}) obtained from N_2 physisorption at −196 °C and from CO_2 adsorption at 25 °C using the BET analysis. c) CO production rate expressed in micromoles per hour normalized per BET SSA obtained from N_2 physisorption or d) from CO_2 adsorption. Multiple repeats have been performed per class of samples. For the commercial $SrTiO_3$, the same batch was used, while for the $SrTi_{1-x}Ga_xO_{3-\delta}$ and $Sr_{1-x}La_xTi_{1-x}Ga_xO_{3-\delta}$ series, three or two different synthesis batches are compared.

which we will investigate below. These results underscore the importance of more research into the intrinsic activity and caution with data interpretation when rationalizing catalytic behavior. Compared to recent literature on photocatalytic CO_2 conversion, our rates compare well with other $SrTiO_3$ based systems that do not employ a co-catalyst on the surface (compare Table S2, Supporting Information). We note, that none of those works have reported their rates normalized to SSA and non-photothermal photohydrogenation reactions with H_2/CO_2 reactants are rare. SSA has been recognized as an important parameter and reported alongside the photocatalytic activity of $SrTiO_3$ for several decades,[33] but it has not yet become a widely adopted standard. This is likely because most studies report photocatalytic activity as the amount of product (in moles or moles per gram of catalyst), typically using stirred particle suspensions. Only recently, activity has been reported per geometric area in the immobilized photocatalyst sheets.[34–36] While such metrics are industrially relevant, they can obscure intrinsic performance comparisons when the surface area changes alongside other material properties. This complicates efforts to establish reliable and standardized benchmarks for photocatalyst performance. Hence, there is a true opportunity to be seized for immobilized photocatalyst systems to report photocatalytic rates per active surface area, which requires the fabrication of films that are on the order of the light penetration depth.

To further understand the intrinsically different photocatalytic activities of the mono- and the co-doped $SrTiO_3$ samples, we embark on a materials characterization analysis commencing with a closer look at their structural properties presented in **Figure 2**. X-ray diffraction (XRD) patterns in Figure 2a confirm that all samples were phase pure, retaining the ABO_3 cubic ($Pm\bar{3}m$) perovskite structure in excellent agreement with the PDF reference card 00-035-0734 for $SrTiO_3$.[9–11] We note that phase purity could be maintained up to a maximum Ga content of 15%,

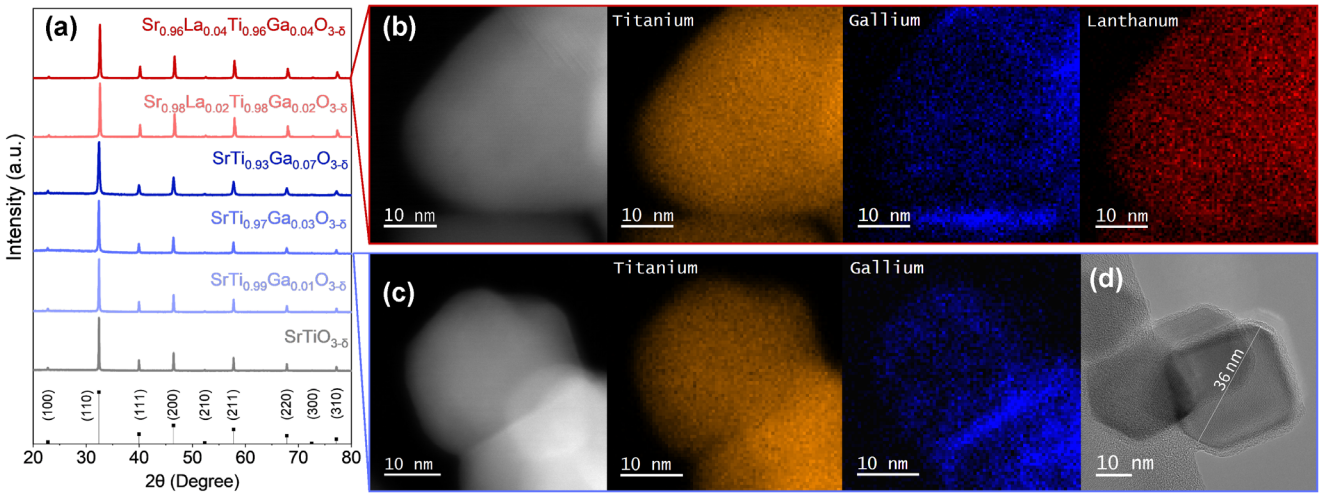

Figure 2. a) XRD patterns for commercial $SrTiO_3$, $SrTi_{1-x}Ga_xO_{3-\delta}$, and $Sr_{1-x}La_xTi_{1-x}Ga_xO_{3-\delta}$ samples, where x is the molar doping concentration. The indexed PDF reference card 00-035-0734 for $SrTiO_3$ is shown for comparison. b) STEM image and corresponding EDS maps of $Sr_{0.96}La_{0.04}Ti_{0.96}Ga_{0.04}O_{3-\delta}$ and c) $SrTi_{0.97}Ga_{0.03}O_{3-\delta}$. See Figure S6 (Supporting Information) for the remaining EDS maps for Oxygen and Strontium. d) Representative HR-TEM image of $SrTi_{0.97}Ga_{0.03}O_{3-\delta}$.

after which secondary phases such as TiO_2 and $SrCO_3$ were noticeable (Section S1, Figure S2, Supporting Information). Crystallite sizes calculated using the Scherrer equation varied in the range of 27–55 nm and were on the same order of magnitude as the nanoparticles in our transmission electron microscopy (TEM) or scanning TEM (STEM) micrographs as shown in Figure 2.

Partial sintering is observed at 900 °C (Figure 2b,c), but nanoparticles predominantly exhibit single-crystalline $SrTiO_3$ character (see Figure 2d and TEM–Fourier Transform, Figure S5, Supporting Information). The energy-dispersive X-ray spectroscopy (EDS) maps show that in both, Ga-doped and La,Ga co-doped samples, Ga segregates to grain boundaries and exhibits a slightly inhomogeneous distribution, with regions of reduced signal intensity. However, interpretation is limited by the low Ga content and counts due to significant drift (10–20 nm) and carbon deposition during the measurement limiting EDS acquisition time and hence counts. We also note that the main EDS peaks for La ($L_{\alpha,1}$ = 4.65 keV and $L_{\alpha,2}$ = 4.63 keV) are masked by the dominant Ti K_α peaks, complicating the analysis. Even though attempts have been made to collect point EDS spectra on visibly darker and lighter regions on a particle (only clearly visible when the images were slightly out of focus, Figure S8, Supporting Information), the obtained Ga-concentrations yielded comparable values within the ≈2% measurement error of EDS so they could not shed light on whether the darker patches are Ga-rich or Ga-poor regions. However, the results confirm that dopant concentrations were consistent with nominal compositions (Figure S8b, Supporting Information). The presence of La and Ga was corroborated by XPS (Figures S9 and S10, Supporting Information). Since the inhomogeneity in Ga concentration occurs in both mono- and co-doped samples, the difference in photocatalytic activity must arise from other factors, in particular because Ga does not appear to be an active site in the CO_2 photohydrogenation reaction as evidenced by SSA-normalized CO production rates which are comparable to undoped $SrTiO_3$ and independent of Ga-concentration.

Figure 3 investigates the optoelectronic properties of our materials, commencing with the photoluminescence spectra for our undoped, doped and co-doped $SrTiO_3$ photocatalysts (Figure 3a). Comparing the undoped $SrTiO_3$ with the Ga-doped samples, a slightly increased intensity can be observed after Ga-doping, but the spectral shape remains unchanged. However, the introduction of La approximately doubles the PL intensity and produces a single sharp PL peak. Normalized PL data in Figure 3b shows this more clearly: the two main PL peaks in the undoped and the Ga-doped $SrTiO_3$ at 3.22 and 3.12 eV are replaced with a single strong PL peak at 3.18 eV in the La,Ga-co-doped samples. The smaller peaks at 3.42 and 2.92 eV are less affected by either dopant. In the following discussion, we will refer to the PL peaks with high intensity and lowest energy as the PL_{minE} peaks (3.18 eV in the La,Ga-co-doped, and 3.12 eV in the Ga-doped $SrTiO_3$). To understand this change in the PL spectral shape, we need to investigate differences in the density of states of the conduction band (CB) and/or the valence band (VB). VB XPS spectra in Figure 3c and Figure S11 (Supporting Information) show the typical VB edge of $SrTiO_3$, as reported previously.[37] A small peak below the bulk of the VB density of states (at a binding energy of ≈10 eV) is visible in the Ga-doped samples, and two peaks (highlighted with asterisks) appear in the La,Ga co-doped samples, which are more evident with higher molar dopant concentration (Figure S11b,c, Supporting Information). Doping with Ga shifts the VB spectrum slightly toward higher binding energies. On the other hand, co-doping with La and Ga slightly shifts the VB spectrum toward lower binding energies with respect to the position of the Fermi level, which is set to zero in these measurements. Since we cannot exclude a change in bandgap, reflectance spectra are shown for Ga-mono-doped samples in Figure 3d and for La,Ga-co-doped samples in Figure 3e, where the insets show Tauc plots to extract their indirect bandgaps. Tauc plots for the remaining samples and those for the extraction of the direct bandgaps are presented in Section S5, Figure S12 (Supporting Information). Apart from minor changes in the bandgap energies

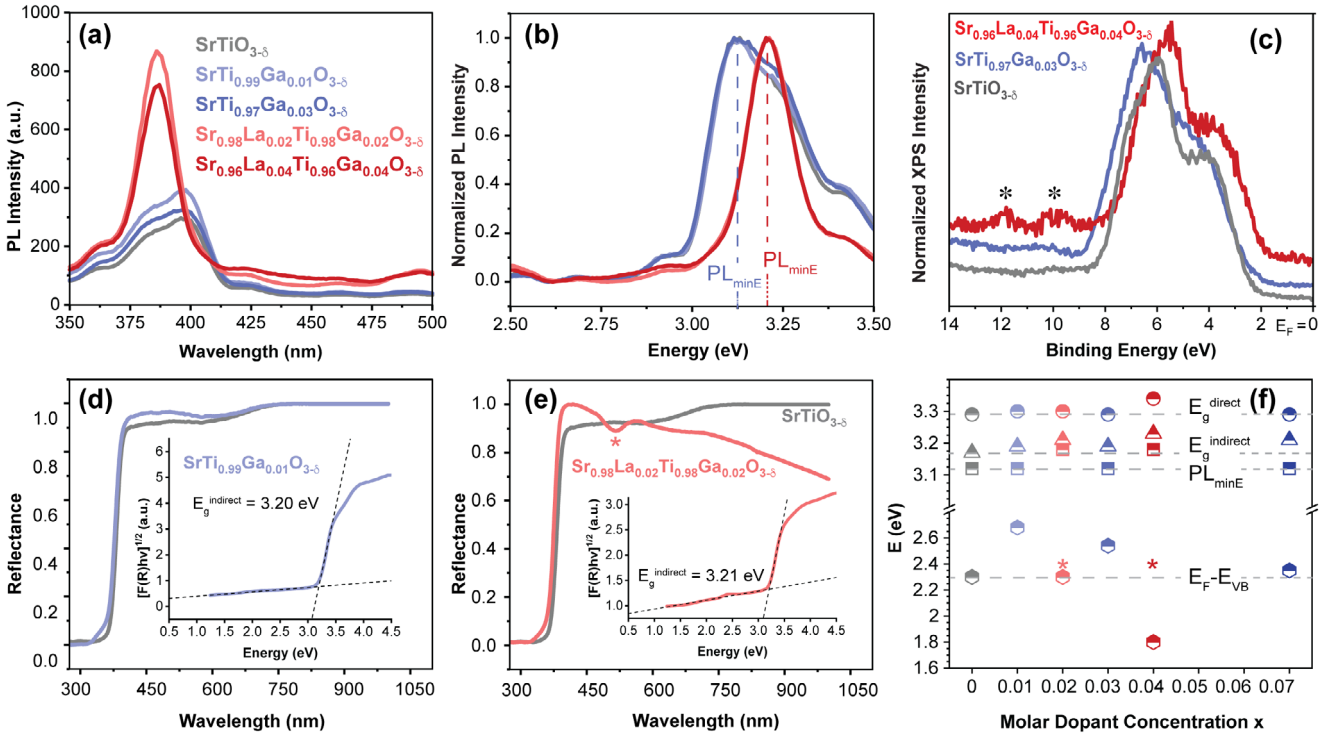

Figure 3. a) PL data of commercial $SrTiO_3$, Ga-doped, and La,Ga-co-doped $SrTiO_3$ in absolute and b) normalized intensities. The PL peak with the highest intensity and lowest energy is marked as PL_{minE}. c) VB-XPS spectra showing the energy difference between the Fermi level (set to zero) and the fitted VB edge. One sub-VB state is visible in Ga-doped $SrTiO_3$ (see also Figure S11, Supporting Information) and two peaks are visible in the La,Ga-co-doped $SrTiO_3$ marked with asterisks. d) Reflectance measurements of a representative Ga-doped $SrTiO_3$ and e) La,Ga-co-doped $SrTiO_3$ overlaid with the reflectance data of commercial undoped $SrTiO_3$ (grey trace). A sub-bandgap absorption feature is highlighted with an asterisk. Insets: Tauc plots for extracting the indirect bandgap. See Figure S12 (Supporting Information) for the remaining samples. f) Energy diagram representation of the direct and indirect bandgaps (E_g^{direct}, $E_g^{indirect}$ from Figure 3d,e and Figure S8, Supporting Information), $PL_{minE,}$ (from Figure 3b) and the E_F-E_{VB} difference (from Figure 3c and Figure S11, Supporting Information) in relation to the molar dopant concentrations in the samples used in this study. The mid-gap absorption feature visible in La,Ga-co-doped samples is indicated with an asterisk.

that will be discussed below, a striking observation in the reflectance data of the La,Ga-co-doped samples is a weak absorption feature at ≈515 nm (2.4 eV), which surprisingly does not increase in intensity with higher dopant concentration of La and Ga (Section S5, Figure S13, Supporting Information). This absorption also gives the co-doped samples a faint blue-greyish tone compared to the bright white powders observed with commercial and Ga-doped $SrTiO_3$. Figure 3f summarizes the above findings in a dopant concentration-dependent energy diagram that illustrates some key observations. First, La,Ga-co-doping slightly increases the indirect bandgap of parent $SrTiO_3$ from 3.17 to 3.21, and 3.23 eV in 2% and 4% La,Ga-doped samples, respectively. To a smaller degree for Ga-mono-doping, the indirect bandgap increases to 3.19 eV for 1% and 3% Ga doping and 3.21 eV in 7% Ga-doped samples. The direct bandgap of $SrTiO_3$ was measured to be 3.29 eV, in accordance with the literature,[37,38] and remains almost unaffected by Ga-mono-doping. Notably, 4% co-doping with La and Ga increases it to 3.34 eV. While these are small variations, they were reproducible with a standard deviation of 0.02 eV and are useful for interpreting the distinct PL spectra of the mono-doped and co-doped samples. For the 4% La,Ga-co-doped sample the PL exhibits a similar energy shift to that seen in the optical bandgaps, i.e., the high intensity lowest energy PL_{minE} peak shifts from 3.12 eV in the undoped and Ga-doped $SrTiO_3$ shifts to 3.18 eV in the La,Ga-co-doped samples – a shift of 60 meV. This closely matches the changes observed in the indirect ($\Delta\ E_g^{indirect} = 3.23\ \text{eV} - 3.17\ \text{eV} = 60\ \text{meV}$) and direct ($\Delta\ E_g^{direct} = 3.34\ \text{eV} - 3.29\ \text{eV} = 50\ \text{meV}$ bandgaps between these samples. However, the direct bandgap difference between the undoped and 2% La,Ga-co-doped samples does not follow this trend. Further analysis of calculated band structure diagrams may clarify the relationship between the PL peak position and the direct vs indirect transitions, especially given their energetic proximity. As seen in Figure 3f, Ga-doping at moderate doping concentrations (1% and 3%) produces significantly more n-type $SrTiO_3$ in accordance with examples of Al^{3+} doping.[39] Lastly, only the La,Ga-co-doped samples show a mid-gap absorption feature with an energy maximum close to the Fermi-level position of the majority of our samples, potentially suggesting a mid-gap state defect equilibrium that causes Fermi-level pinning. Interestingly, the 4% La,Ga-co-doped sample shows a near-intrinsic Fermi level position.

To further understand these results, we turn to density functional theory (DFT) computed for Ga-doped and La,Ga-co-doped $SrTiO_3$ samples with doping concentrations of 12.5% respectively (**Figure 4**). The high doping concentrations of 12.5% resulted from a 2 × 2 × 2 simulation cell with 40 atoms chosen to assess

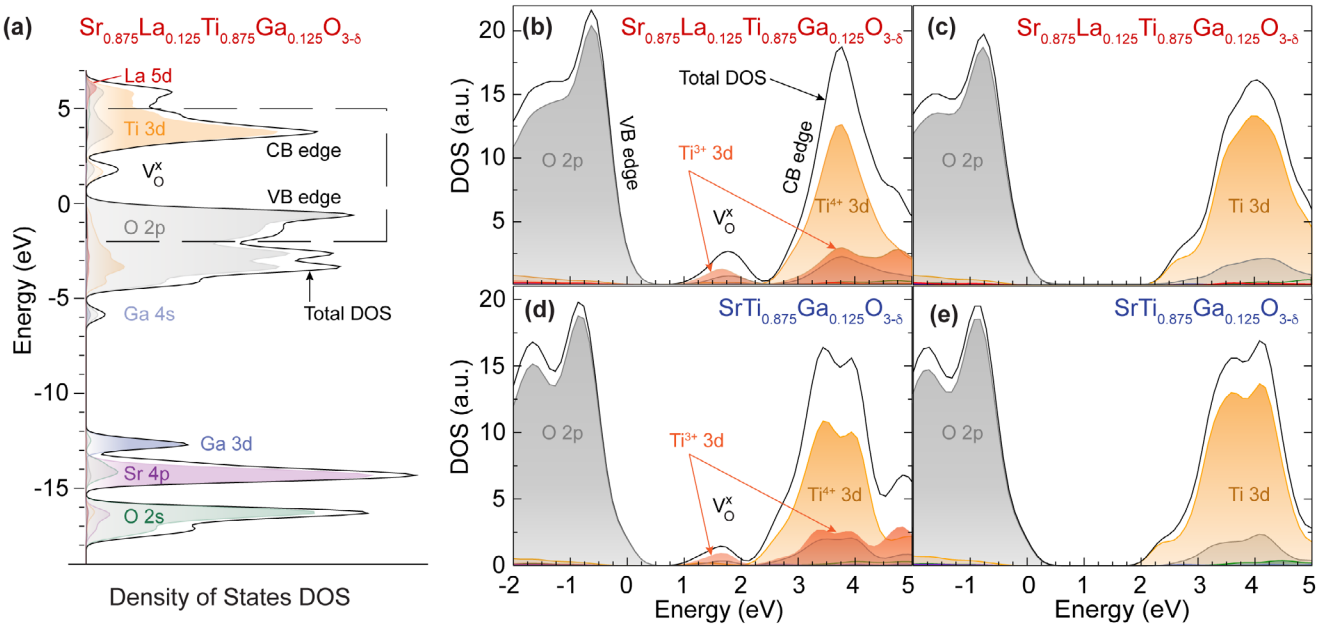

Figure 4. Computed density of states (DOS) diagrams of La,Ga co-doped and Ga-mono-doped materials. a) Main atomic contributions to different regions of the DOS, including semi-core states, of the co-doped sample showing Ga and La contributions as well as the presence of an uncompensated oxygen vacancy V_O^x (color center defect). b–e) DOS around the bandgap, for charge uncompensated (b,d) and charge compensated (c,e) cells in the presence of doping and oxygen vacancies. Two Ti 3d species are shown in (b,d) as a result of the uncompensated oxygen vacancy.

four different configurations with sufficient computational resources. However, calculations using a 3 × 3 × 3 cell, resulting in an experimentally relevant dopant concentration of 3.7%, did not significantly change the outcome (see Figure S14a, Supporting Information). Figure 4a shows the density of states (DOS) energy diagram for a La,Ga-co-doped sample with the VB edge set to zero by convention. This diagram illustrates that the CB edge is composed predominantly of Ti 3d states, and the VB edge of O 2p states, as expected.[38] Ga 3d states are located deep in the VB followed by Sr 4p and O 2s states, which have little to no contribution to bonding in the range of the band edges and can be considered semi-core-like. Ga 4s states interact with the O 2p states in a bonding interaction seen ≈6 eV below the top of the VB and their antibonding interaction disappears in the high DOS near the CB edge. Empty La 5d states are found ≈6 eV above the VB edge in the CB. Occupied Ga 4p states and La d states are hidden by the large DOS of O 2p and Ti 3d states at the bottom of the VB edge (above the Ga 4s states) shown in Figure S14b (Supporting Information). Figure 4a also accounts for the presence of uncompensated oxygen vacancies, denoted as V_O^x, which carry their two electrons (F-center defect), forming a mid-gap state that is partially filled with electrons to which both the Ti 3d and O 2p states contribute. Similar energies for mid-gap absorption states have been measured and simulated in other oxides with similar bandgaps, such as ZnO, ZrO_2, and TiO_2 and have been attributed to oxygen vacancies as well.[40] The effect of electron occupancy in the oxygen vacancies on the DOS energy band diagram is further explored in Figures 4b–e. Figure 4b is an extract of Figure 4a (marked by the box), zooming in on the bandgap region. Whereas Figure 4a shows the contribution of all Ti 3d states to the total DOS, Figure 4b distinguishes the contribution from Ti^{4+} species and Ti^{3+} species. It is now apparent that Ti^{3+} 3d states contribute to the V_O^x related states as well as to the CB DOS, whereas (empty) Ti^{4+} 3d states only contribute to the CB. If the oxygen vacancy is fully oxidized (or, in other words, fully compensated), it does not carry electrons and hence, the mid-gap state and also the Ti^{3+} species disappear (Figure 4c). Very similar pictures can be drawn for the Ga-mono-doped samples (Figures 4d,e). Also here, the occupancy of the oxygen vacancy dictates the formation of a mid-gap state. The F-center defect we assess here can be interpreted as a $Ti_{Ti}^x - V_O^x - Ti_{Ti}^x \leftrightarrow Ti_{Ti}' - V_O^{\cdot\cdot} - Ti_{Ti}'$ complex with two resonance forms, indicating the shared electrons between the oxygen vacancy and its Ti neighbors.

Before we relate these band diagrams to our data, we can make use of the Kröger–Vink notation in the following set of equations to elucidate how La and Ga doping could affect the formation of oxygen vacancies and their occupancy in light of the Fermi-level position in our samples.

The commercial $SrTiO_3$ is n-type, which is typically attributed to the presence of oxygen vacancies that function as electron donors via

$$V_O^x \rightleftharpoons V_O^{\cdot\cdot} + 2e_{cb}' \quad (1)$$

forming the above-mentioned $Ti_{Ti}^x - V_O^x - Ti_{Ti}^x \leftrightarrow Ti_{Ti}' - V_O^{\cdot\cdot} - Ti_{Ti}'$ complex by donating these electrons to the Ti 3d CB and forming Ti^{3+} 3d states. Singly-occupied oxygen vacancies might occur as well, but here we focus on the two extremes – the fully ionized and the fully occupied oxygen vacancy for simplicity – since we do not see evidence for the singly-occupied vacancy in our experiments or calculations.

Considering Ga doping under oxygen-poor conditions, likely present during our synthesis under light air flow, we can write:

$$Ga_2O_3 \xrightarrow[(or\ TiO_2)]{SrTiO_3} 2Ga_{Ti}^{x} + 3O_O^{x} + V_O^{x} \quad (2)$$

to show that Ga is incorporated on a Ti lattice site, creating an oxygen vacancy to fulfill the stoichiometry of the lattice (here considering only B-site doping, i.e., TiO_2 stoichiometry). Formally, Ga^{3+} is oxidized to fulfill the neutral condition of the lattice site (the equivalent of a Ti^{4+} state), whereas the oxygen vacancy is charge-neutral, carrying those two electrons provided by the Ga^{3+} upon its formal oxidation. Ga could act as an electron acceptor, and oxidize the top of the VB:

$$2Ga_{Ti}^{x} + O_O^{x} \rightleftharpoons 2Ga_{Ti}^{'} + V_O^{\cdot\cdot} + \frac{1}{2}O_2 \quad (3)$$

If the Ga site is near an F-center, it can equilibrate via

$$2Ga_{Ti}^{x} + V_O^{x} \rightarrow 2Ga_{Ti}^{'} + V_O^{\cdot\cdot} \quad (4)$$

ionizing the oxygen vacancy instead. In both cases, Ga seems to form oxidized oxygen vacancies instead of creating mobile VB holes that would induce p-type conductivity, which was observed in Rh^{3+}-doped $SrTiO_3$ (likely due to significant Rh 4d character of the VB edge).[37] This is in line with our observation that Ga-doping slightly raises the Fermi level at low concentrations (as per Equations 1–3) and remains close to the values of undoped commercial $SrTiO_3$ in higher doped samples via the compensation equilibrium in Equation (4) (Figure 3f; Figure S11, Supporting Information).

La is incorporated very likely on the A-site due to its size, giving rise to the following equation:

$$La_2O_3 \xrightarrow[(or\ SrO)]{SrTiO_3} 2La_{Sr}^{x} + 2O_O^{x} + \frac{1}{2}O_2 \quad (5)$$

In the presence of Ga, equilibration would then occur via charge compensation

$$2La_{Sr}^{x} + 2Ga_{Ti}^{x} \xrightarrow{SrTiO_3} 2La_{Sr}^{\cdot} + 2Ga_{Ti}^{'} \quad (6)$$

leaving the oxygen vacancy created upon Ga-doping (Equation (2)) in a neutral (unionized) state. Overall, we obtain:

$$Ga_2O_3 + La_2O_3 \xrightarrow{SrTiO_3} 2La_{Sr}^{\cdot} + 2Ga_{Ti}^{'} + 5O_O^{x} + V_O^{x} + \frac{1}{2}O_2 \quad (7)$$

O_2 could be introduced into the lattice, annihilating the neutral oxygen vacancy as per Equation (8):

$$V_O^{x} + \frac{1}{2}O_2 \rightleftharpoons O_O^{x} \quad (8)$$

Equation (8) would lead to a more stoichiometric and thus intrinsic material, and could explain the Fermi level in the 4% La,Ga-co-doped sample, which is very close to the middle of the bandgap (Figure 3f).

Even if La is not able to equilibrate with Ga via Equations (6) and (7), it could compensate with an ionized oxygen vacancy as follows

$$2La_{Sr}^{x} + V_O^{\cdot\cdot} \xrightarrow{SrTiO_3} 2La_{Sr}^{\cdot} + V_O^{x} \quad (9)$$

also creating a color center.

Now we can attempt to draw a *qualitative* comparison between the DFT-calculated DOS diagrams of Ga-doped and La,Ga-co-doped $SrTiO_3$ samples presented in Figure 4 and our experimental results from VB-XPS, UV–vis, and PL spectra presented in Figure 3.

Figure 5 shows this comparison with the computational results plotted on the left for the mono- and co-doped $SrTiO_3$ in the presence of F-centers, V_O^{x} (c.f. Figure 4a,b,d) and the experimental results of our doped samples on the right. We note that the VB edge was set to zero in the left-hand side DOS data as well as in the right-hand side experimental XPS data and the PL data was plotted with respect to this zeroing of the VB edge. This allows us to see that our experimental and theoretical data mirror one another rather well. The VB XPS spectra are in good agreement with the DFT calculations with the latter showing more fine structure. We can compare the state that is attributed to Ga 4s in the DFT calculations to a small peak in the VB XPS spectra below the main O 2p VB even though the binding energies do not fully match up as DFT calculates a narrower VB (≈5 eV) compared to the one we observe in our VB XPS data (≈6 eV, see Figure 3c). However, a discrepancy is observed in the La,Ga-doped sample with 4% co-doping which shows two small peaks below the main VB whereas in the calculated DOS only the Ga 4s states are visible. While this needs further experimental verification, we find that the large VB DOS also shows contributions from the Ga p and La d states hidden within the O 2p-based lower VB edge (Figure S14b, Supporting Information). These might be more stabilized than our DFT calculations predict, accounting for the second peak in the La,Ga-co-doped samples.

Comparing the PL data with our DFT CB states, we observe that they also *qualitatively* mirror one another well, even though our DFT calculations report ground-state DOS.

Looking at the region marked with (A), we observe that both, the DFT-calculated DOS (left) and the PL spectrum of Ga-doped $SrTiO_3$ (right) show the two strong peaks discussed as the 3.12 and 3.21 eV peaks in Figure 3b whereas the DOS and PL spectra of the La,Ga-co-doped samples show both only one strong peak situated between those two peaks of the Ga-doped $SrTiO_3$. The PL_{minE} peak at 3.18 eV in the La,Ga-co-doped samples is very close to the direct and indirect bandgaps as determined via Tauc plots (Figure 3), and so by comparison, we link the radiative recombination process (A) to the Ti 3d CB states of Ti^{4+} species surrounded by lattice oxygen ($Ti_{Ti}^{x} - O_O^{x}$). These states are likely populated upon excitation and radiatively recombine with the O 2p VB holes, emitting at 3.18 eV. As such, it could be seen as band-to-band recombination or as near-band-edge emission, potentially phonon-mediated as suggested previously.[41,42] Similarly, in the Ga-mono-doped samples, the two largest DOS peaks

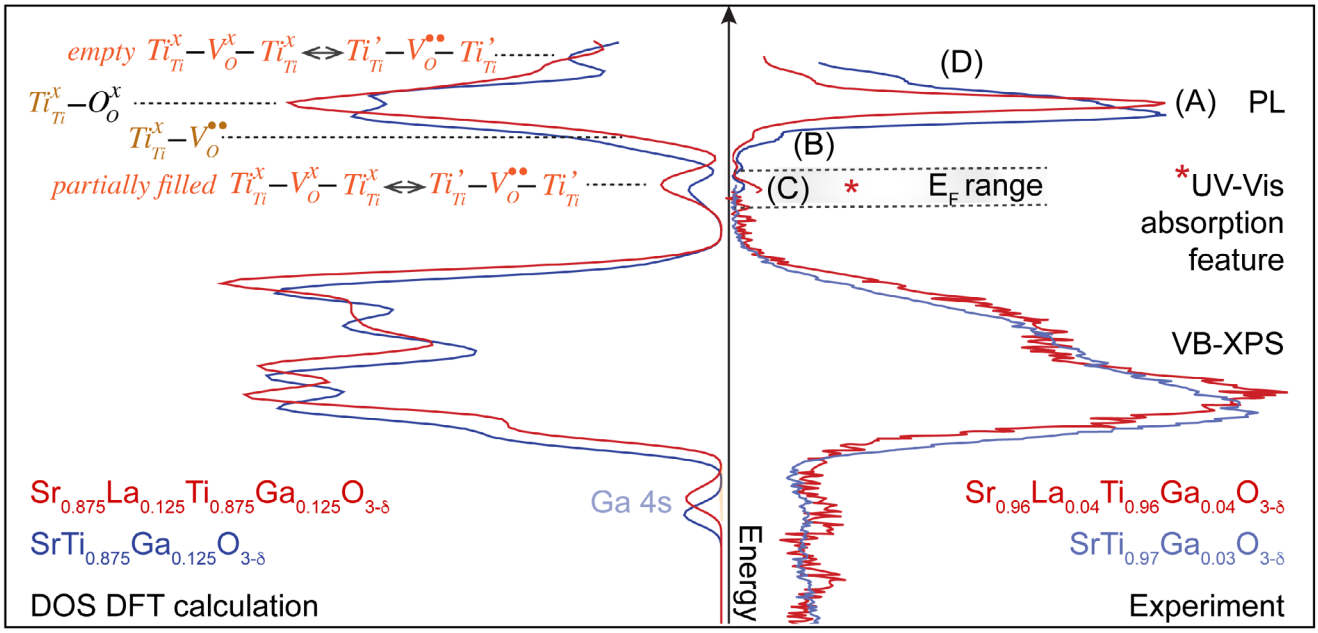

Figure 5. Qualitative comparison of density of states (DOS) DFT calculations (left) and valence band (VB) XPS, UV–vis and PL experiments (right) for Ga-mono-doped (blue) and La,Ga-co-doped (red) samples. DFT calculations are shown for dopant concentrations of 12.5% for samples with uncompensated oxygen vacancies. For assignments of PL peaks A–D) and the DOS contributions, please refer to the main text. Note also the Fermi level range of most samples (marked in grey) and the asterisk (* in red) that marks the UV–vis absorption peak at 2.4 eV visible in Figures 3e,f.

on the left can be correlated to the two most intense PL peaks at 3.12 and 3.21 eV on the right. Currently, it is not clear from our calculations and experiments why the Ga-mono-doped and the undoped $SrTiO_3$ samples show these two distinct peaks in contrast to the sharp peak in the co-doped samples. We speculate that this might be related to lattice distortions upon doping with La, affecting the band structure diagram, which will be investigated in future work.

There is a lower energy shoulder peak at 2.92 eV marked as (B) in Figure 5, which can be linked to the Ti 3d states that also form a shoulder at the bottom of the CB edge DOS. This shoulder is more prominent in the compensated materials with ionized oxygen vacancies (Figure 4c,e). A blue emission at 2.8 eV in $SrTiO_3$ has been previously assigned to the recombination of an electron in a singly positive electron polaron-$V_O^{\cdot\cdot}$ complex with a VB hole.[43] This agrees with our assignment (B), that is, the shoulder peak in the DOS is likely created by a Ti lattice site adjacent to an ionized oxygen vacancy, $V_O^{\cdot\cdot}$, giving the Ti a higher effective nuclear charge, thereby lowering its energy compared to a Ti site in a stoichiometric lattice. This can be viewed as a $Ti_{Ti}^{x} - V_O^{\cdot\cdot}$ doubly positively charged complex, which can form the singly positively charged complex mentioned in literature upon excitation of a VB-electron, causing the emission at 2.92 eV when recombining back to the ground state. This emission shoulder is present in the mono-doped samples and, though weaker, is also observed in the co-doped samples, suggesting that our materials have a contribution from both the DOS of the materials with uncompensated and those with compensated (ionized) oxygen vacancies. This is also corroborated by the weak PL peak at 2.5 eV present in the La,Ga-co-doped samples, but also weakly visible in the Ga-mono-doped (and undoped) samples (Figures 3b and 5). This peak is marked as process (C), which we cannot easily assign to a specific recombination process in our diagrams, as it is also controversially debated in the literature. However, we can state that the presence of neutral oxygen vacancies (F-centers) forming the mid-gap state is likely causing this emission and also the absorption feature, which falls into the same energy range (marked in Figure 5 by the same asterisk we used in the UV–vis reflectance spectra in Figure 3e). The absence of the absorption feature at 2.4 eV (Figure 3d) and also the weaker PL peak at 2.5 eV in the Ga-mono-doped samples (Figure 3a,b) suggests that the concentration of V_O^{x} is lower than in the La,Ga-co-doped samples, as Equations (3), (4), and (7) predict. To further corroborate our assignment of the 515 nm feature to the oxygen vacancy equilibrium, we exploited the reaction in Equation (8), comparing the UV–vis spectra of a La,Ga-co-doped sample pre- and post-annealing at 500 °C in high-pressure (50 bar) oxygen atmosphere (Figure S15a, Supporting Information). The mobility of oxygen and oxygen vacancies through the lattice only becomes appreciable at 750 K (or ≈477 °C).[44] After 6 h, the 515 nm feature decreased its intensity to 30% of the original peak area. We subsequently re-annealed the sample used in Figure S15a (Supporting Information) at 900 °C in air, where oxygen and oxygen vacancy mobilities are expected to be higher. Figure S15b (Supporting Information) shows that the sharp 515 nm absorption feature is no longer identifiable, and instead, a broader but shallow dip in reflectance can be observed across the visible/NIR region. These experiments showcase the sensitivity of the 515 nm feature to the oxygen environment under temperatures that allow for mobile lattice oxygen and oxygen vacancies.

Interestingly, Figure 5 also shows that for the majority of our samples, the Fermi-level is located in the range of this V_O^{x}-caused mid-gap state, which we assigned to the $Ti_{Ti}^{x} - V_O^{x} - Ti_{Ti}^{x} \leftrightarrow Ti_{Ti}' - V_O^{\cdot\cdot} - Ti_{Ti}'$ complex. This would suggest a partially

filled state (e.g., resulting from a Jahn–Teller-stabilized Ti t_{2g} electron interacting with O 2p states), which pins the Fermi level and is likely sensitive to the oxygen vacancy redox behavior according to Equation (1).

Finally, the other shoulder peak at 3.42 eV in the PL (marked as process (D) in Figure 5), could then be assigned to the empty Ti 3d CB states formed by Ti^{3+} sites as seen in Figure 4b,d. This is supported by the DOS diagrams in Figure 4c,e for fully ionized oxygen vacancies that lack the presence of this peak in the upper CB and is in good agreement with previous studies.[45]

Relating our findings on the defect chemistry and electronic structure of doped $SrTiO_3$ (Figures 3–5) with their photocatalytic performance in the CO_2 hydrogenation reaction (Figure 1), we observe a correlation between enhanced CO evolution rates and key material features in the La,Ga-co-doped photocatalysts such as sharper and more intense photoluminescence (PL) peaks and the presence of F-centers (oxygen vacancies filled with electrons or, using the Kröger-Vink notation, $Ti_{Ti}^{x} - V_O^{x} - Ti_{Ti}^{x} \leftrightarrow Ti_{Ti}' - V_O^{\cdot\cdot} - Ti_{Ti}'$ complexes).

While sharper and stronger PL signals are commonly interpreted as indicators of improved semiconducting properties, as shown in many photovoltaic works,[46] F-centers have often been considered detrimental to photoactivity. For example, in water splitting photoelectrodes, oxygen vacancies and mid-gap states have been associated with charge carrier recombination and reduced performance,[47–50] and improved photocatalytic hydrogen evolution activity in $SrTiO_3$ was previously attributed to the suppression of Ti^{3+} mid-gap recombination centers.[22–24] However, our results studying the CO_2 photohydrogenation reaction with H_2 as a reductant, rather than water, might offer a different perspective. Our results suggest that the presence of F-centers does not appear to be detrimental to the activity and thus, they do not seem to function as trap states. This could be due to the faster kinetics of H_2 oxidation, in contrast to the sluggish oxygen evolution reaction, in combination with the small size of our nanoparticulate photocatalysts, both facilitating fast hole extraction. However, further studies are needed to unravel if and how F-centers enhance photocatalytic rates. For example, it should be investigated if they might act as catalytically active sites or might enhance the reaction rate indirectly through decreasing the concentration of electron localization sites (e.g., in $V_O^{\cdot\cdot} - Ti_{Ti}^{x}$ states just at the bottom of the conduction band, as shown in Figures 4c,e, and 5).

3. Conclusion

Our work crystallizes a few key points to be considered in future studies in photocatalysis. First, we emphasize that any insights gained into structure-function correlations were only made possible by normalizing photocatalytic activity to the specific surface area (SSA) of our catalysts, which allowed us to disentangle improvements due to increased surface area from those arising from enhancements in opto-electronic properties. This is only possible if the light penetration depth is on the order of the film thickness. In our study, we used thin nanoparticle films inspired by the photocatalyst sheet device.[51] However, we acknowledge that light penetration depth is not clearly defined in stirred catalyst suspensions, and hence, accounting for surface area might not be easily feasible or suitable for those systems.

Second, plotting our DFT results alongside experimental data, including photoluminescence (PL), UV–vis spectroscopy, and valence band X-ray photoelectron spectroscopy (VB-XPS), proved extremely valuable in constructing an experimentally supported picture of the electronic structure. This comparative analysis revealed a striking mirror image relationship: the PL spectra provided insights into the shape of the conduction band edge in our $SrTiO_3$ samples, while the combined interpretation of VB-XPS, PL, and UV–vis data not only mapped the VB and defect levels but also clarified that the Fermi level is pinned at the F-center. We encourage the construction of similar experimentally supported DOS diagrams to see if PL spectra are also a useful metric to trace the conduction band states in other materials and to understand the energetics of defect states such as color centers and their effect on Fermi level pinning in more detail.

Third, we identify two material properties that seem to play a role in enhancing the activity of our La,Ga-co-doped $SrTiO_3$ photocatalysts in the CO_2 photohydrogenation reaction, namely, a distinct narrow PL spectral shape of higher intensity, and the presence of a mid-gap state, which we attribute to F-centers (neutral oxygen vacancies). Although further mechanistic insights are needed to fully clarify the role of F-centers in CO_2 photohydrogenation, our findings suggest that color centers do not contribute negatively to CO_2 photohydrogenation activity of our catalysts and hence do not seem to function as detrimental hole or electron traps.

Finally, we highlight the CO_2 photohydrogenation reaction with H_2 as the reductant as a versatile reaction of industrial relevance. It is typically explored only in thermal or photothermal heterogeneous catalysis. As such, there is an opportunity to develop tailored photocatalysts in future works through the understanding of key material properties. The methodology developed in this work for normalizing the photocatalytic activity of immobilized, doped $SrTiO_3$ by their SSA enables a more direct assessment of intrinsic electronic effects. This approach provides a foundation for the rational design of tailored photocatalysts for CO_2 photohydrogenation and for further investigation of the role of F-centers.

4. Experimental Section

Synthesis, photocatalysis, and surface area experimental procedures are reported in Sections S1 and S2 (Supporting Information).

XRD data were collected over a 2θ range of 20°–80° with a step size of 0.02° and 24.77 s $step^{-1}$ with a PanAnalytical MPD operated at 40 kV and 40 mA using Cu K_α radiation (λ = 1.5419 Å). To estimate the mean crystallite size, the Scherrer equation was applied $D_{Scherrer} = \frac{K\lambda}{\beta \cos\theta}$, where $D_{Scherrer}$ is the mean crystallite size. K is a shape factor set to 0.9, λ is the wavelength of the X-rays (0.154 nm for Cu K_α radiation), β is the full width at half maximum (FWHM) of the peak, and θ is the Bragg angle. The peaks were fitted using a Gaussian function, and LaB_6 was chosen as the standard to account for the instrumental broadening.

TEM and STEM-EDS characterization in Figure 2 was carried out using a JEM-ARM300F2 GRAND ARM microscope equipped with double SSD EDS detectors at 300 kV acceleration voltage. The sample was drop-casted onto a TEM copper grid with carbon support, which was mounted in a High-Count-Analytical Double Tilt holder to optimize for EDS counts and reduce instrument spurious signals. TEM images in Figure S5 (Supporting Information) were acquired with a JEOL2100 operated at 200 kV. Images and EDS spectra in Figure S8 (Supporting Information) were acquired with a JEOL2100F equipped with an EDS detector. FFT analysis has been carried out using the software ImageJ and Crystal Maker. During the optimization

of the synthesis method, samples with several Ga concentrations were synthesized and exhibited structural and electronic properties consistent with the rest of the series. Representative Ga-doped $SrTiO_3$ samples were used in microscopy characterization, justified by the fact that across the 1–7 mol% Ga series of samples, the SSA-normalized rate of CO photoevolution remains unchanged.

XPS data were taken with a Thermo Scientific K-alpha+ using monochromatic Al K_α X-ray radiation with $h\nu = 1486.6$ eV. For the analysis, a very thin layer of sample powder was loaded on a carbon tape. Sample charging was minimized by using a flood gun. Charge correction of the samples was done by referencing to the adventitious carbon in C 1s peak with a binding energy of 284.8 eV. CasaXPS suite was used for peak fitting. The E_{VB}-E_F separation was calculated from the intersection of the linear regressions of the linear region of the valence band and the background.

UV–vis measurements were carried out at room temperature on a UV-2600 Shimadzu instrument using an integrating sphere to collect diffuse reflectance spectra from dry powders loaded in a 2 mm thin quartz cuvette. Reflectance data was converted to the equivalent of the absorption coefficient using the Kubelka–Munk equation, $F(R) = \frac{k}{s} = \frac{(1-R)^2}{(2R)}$, to generate Tauc plots, where k is the absorption coefficient, s is defined as the scattering coefficient and R is the diffuse reflectance of an opaque layer of powder referenced to $BaSO_4$ (where opaque means that there is no transmittance of light in the spectral region). The bandgap is calculated from the Tauc plot $\left(F(R)^* h\nu\right)^\gamma = B\left(h\nu - E_g\right)$ extracting the indirect ($\gamma = 1/2$) and direct ($\gamma = 2$) bandgaps by intersecting the linear regressions of the slope and the background.

PL was collected with a Cary Eclipse Fluorescence Spectrophotometer (Agilent Technologies) instrument with a Xenon flash lamp as a light source. Dry powders in a 2 mm quartz cuvette were excited with 295 nm, and emission spectra were collected over a range of 350–500 nm at room temperature in air.

DFT Spin-polarized density functional theory (DFT) simulations were carried out with the Quantum-ESPRESSO code.[52,53] Vanderbilt ultrasoft pseudopotentials were employed,[54] and wavefunctions were described with a plane-wave basis set up to energy cutoffs of 40 and 480 Ry for wavefunctions and densities, respectively. Exchange and correlation were treated at the level of Generalized-Gradient Approximation (GGA) in the formulation of Perdew, Burke, and Ernzerhof (PBE).[55] Strong Coulomb interaction due to the localized 3d states of Titanium was taken into account with a Hubbard U correction,[56–58] with a value of U = 4.2 eV taken from the literature.[59,60] Van der Waals interaction was included through Grimme's D3 semi-empirical potential.[61] Metallic occupations were enforced with a Marzari–Vanderbilt scheme[62] and a smearing of 0.02 Ry. Integrations in the first Brillouin zone were performed on grids equivalent to (4 × 4 × 4) k-points in the unit cell. All atomic positions and cell parameters were relaxed until forces were smaller than 10^{-3} a.u. To distinguish between Ti^{3+} and Ti^{4+} species, the density of states was projected on (pseudo)atomic orbitals of individual atoms which is used to calculate the Lowdin pseudo-atomic charge and spin by integrating all projections on all orbitals of an atom. It is possible then to distinguish Ti^{4+} and Ti^{3+} either from the change in charge or in spin. However, it is commonly observed that changes in Lowdin charges are usually small (≈0.1 electronic charges), while the spin delivers a much clearer signature of the oxidation state of the titanium atoms, with Ti^{4+} having a total spin smaller than 0.1 while Ti^{3+} can be distinguished via a spin between 0.9 and 1, in agreement with the ideal picture of a reduced titanium ion.[63]

Supporting Information

Supporting Information is available from the Wiley Online Library or from the author.

Acknowledgements

D.B. and B.S. contributed equally to this work. The authors thank the Departments of Materials and Chemistry at the University of Oxford and Imperial College London for access to XPS, XRD, EM, XPS and BET facilities. Specifically, the authors acknowledge the use of characterization facilities within the David Cockayne Center for Electron Microscopy (Oxford, Department of Materials) alongside financial support provided by the Henry Royce Institute (Grant EP/R010145/1). The authors thank the McCulloch group, and particularly Dr. F. Moruzzi, for providing access to the photocatalytic setup, Prof. A. Kafizas for access to the XRD and PL systems and Prof. M. Hayward along with Ms. J. Neill and Mr. W. Doel for access, training and assistance with high-pressure oxygen annealing experiments. B.S. acknowledges funding from the EPSRC Oxford Inorganic Chemistry for Future Manufacturing Center for Doctoral Training (EP/S023828/1). This work was supported by funding from the Imperial College Research Fellowship and the EPSRC [grant number EP/Z000343/1 Frontier Research Guarantee for the ERC Starting Grant]. All DFT calculations were performed on the ICTP cluster Argo and the Leonardo machine at CINECA.

Conflict of Interest

The authors declare no conflict of interest.

Data Availability Statement

The data presented in the main body and the Supporting Information of this paper are available on Zenodo at https://doi.org/10.5281/zenodo.17324613 and can be used under the Creative Commons Attribution 4.0 International license.

Keywords

CO_2 reduction photocatalyst, color centers, electronic structure of $SrTiO_3$, oxygen vacancy defects, surface area-normalized activity

Received: May 12, 2025
Revised: October 14, 2025
Published online:

[1] T. Takata, J. Jiang, Y. Sakata, M. Nakabayashi, N. Shibata, V. Nandal, K. Seki, T. Hisatomi, K. Domen, *Nature* **2020**, *581*, 411.
[2] K. Maeda, K. Teramura, D. Lu, T. Takata, N. Saito, Y. Inoue, K. Domen, *Nature* **2006**, *440*, 295.
[3] S. Kawasaki, R. Takahashi, K. Akagi, J. Yoshinobu, F. Komori, K. Horiba, H. Kumigashira, K. Iwashina, A. Kudo, M. Lippmaa, *J. Phys. Chem. C* **2014**, *118*, 20222.
[4] Q. Wang, T. Hisatomi, Q. X. Jia, H. Tokudome, M. Zhong, C. Z. Wang, Z. H. Pan, T. Takata, M. Nakabayashi, N. Shibata, Y. B. Li, I. D. Sharp, A. Kudo, T. Yamada, K. Domen, *Nat. Mater.* **2016**, *15*, 611.
[5] Y. Shen, C. Ren, L. Zheng, X. Xu, R. Long, W. Zhang, Y. Yang, Y. Zhang, Y. Yao, H. Chi, J. Wang, Q. Shen, Y. Xiong, Z. Zou, Y. Zhou, *Nat. Commun.* **2023**, *14*, 1117.
[6] T. Jia, Y. Hao, H. Hao, Z. Zeng, *RSC Adv.* **2024**, *14*, 6360.
[7] M. V. Dozzi, E. Selli, *J. Photochem. Photobiol., C* **2013**, *14*, 13.
[8] I. E. L. Stephens, K. Chan, A. Bagger, S. W. Boettcher, J. Bonin, E. Boutin, A. K. Buckley, R. Buonsanti, E. R. Cave, X. Chang, S. W. Chee, A. H. M. da Silva, P. de Luna, O. Einsle, B. Endrődi, M. Escudero-Escribano, J. V. Ferreira de Araujo, M. C. Figueiredo, C. Hahn, K. U. Hansen, S. Haussener, S. Hunegnaw, Z. Huo, Y. J. Hwang, C. Janáky, B. S. Jayathilake, F. Jiao, Z. P. Jovanov, P. Karimi, M. T. M. Koper, et al., *J. Phys.: Energy* **2022**, *4*, 042003.
[9] Y. Zhou, B. Bowers, A. Bagger, G. Yang, L. Steier, M. P. Ryan, I. E. L. Stephens, *ACS Energy Lett.* **2025**, *10*, 4324.

[10] Q. Yang, Y. Wang, Q. Tian, X. Li, A. Pan, M. Zhao, Y. Zhu, T. Wu, G. Fang, *J. Mater. Chem. A* **2024**, *12*, 7207.
[11] Z. Geng, X. Kong, W. Chen, H. Su, Y. Liu, F. Cai, G. Wang, J. Zeng, *Angew. Chem., Int. Ed.* **2018**, *57*, 6054.
[12] B. Liu, C. Li, G. Zhang, X. Yao, S. S. C. Chuang, Z. Li, *ACS Catal.* **2018**, *8*, 10446.
[13] X. Ren, Y. Gao, L. Zheng, Z. Wang, P. Wang, Z. Zheng, Y. Liu, H. Cheng, Y. Dai, B. Huang, *Surf. Interfaces* **2021**, *23*, 100923.
[14] M. Ghoussoub, M. Xia, P. N. Duchesne, D. Segal, G. Ozin, *Energy Environ. Sci.* **2019**, *12*, 1122.
[15] J. Zhai, Z. Xia, B. Zhou, H. Wu, T. Xue, X. Chen, J. Jiao, S. Jia, M. He, B. Han, *Nat. Commun.* **2024**, *15*, 1109.
[16] Z. Zhang, C. Mao, D. M. Meira, P. N. Duchesne, A. A. Tountas, Z. Li, C. Qiu, S. Tang, R. Song, X. Ding, J. Sun, J. Yu, J. Y. Howe, W. Tu, L. Wang, G. A. Ozin, *Nat. Commun.* **2022**, *13*, 1512.
[17] G. Chen, R. Gao, Y. Zhao, Z. Li, G. I. N. Waterhouse, R. Shi, J. Zhao, M. Zhang, L. Shang, G. Sheng, X. Zhang, X. Wen, L.-Z. Wu, C.-H. Tung, T. Zhang, *Adv. Mater.* **2018**, *30*, 1704663.
[18] F. Moruzzi, W. Zhang, B. Purushothaman, S. Gonzalez-Carrero, C. M. Aitchison, B. Willner, F. Ceugniet, Y. Lin, J. Kosco, H. Chen, J. Tian, M. Alsufyani, J. S. Gibson, E. Rattner, Y. Baghdadi, S. Eslava, M. Neophytou, J. R. Durrant, L. Steier, I. McCulloch, *Nat. Commun.* **2023**, *14*, 3443.
[19] Y. Zhang, X. Wu, Z.-H. Wang, Y. Peng, Y. Liu, S. Yang, C. Sun, X. Xu, X. Zhang, J. Kang, S.-H. Wei, P. F. Liu, S. Dai, H. G. Yang, *J. Am. Chem. Soc.* **2024**, *146*, 6618.
[20] V. M. Goldschmidt, *Naturwissenschaften* **1926**, *14*, 477.
[21] R. D. Shannon, *Acta Crystallogr. A* **1976**, *32*, 751.
[22] R. Li, T. Takata, B. Zhang, C. Feng, Q. Wu, C. Cui, Z. Zhang, K. Domen, Y. Li, *Angew. Chem., Int. Ed.* **2023**, *62*, 202313537.
[23] Z. Zhao, R. V. Goncalves, S. K. Barman, E. J. Willard, E. Byle, R. Perry, Z. Wu, M. N. Huda, A. J. Moulé, F. E. Osterloh, *Energy Environ. Sci.* **2019**, *12*, 1385.
[24] T. Takata, K. Domen, *J. Phys. Chem. C* **2009**, *113*, 19386.
[25] A. Bagger, W. Ju, A. S. Varela, P. Strasser, J. Rossmeisl, *ChemPhysChem* **2017**, *18*, 3266.
[26] U. Terranova, F. Viñes, N. H. de Leeuw, F. Illas, *J. Mater. Chem. A* **2020**, *8*, 9392.
[27] A. Crake, K. C. Christoforidis, R. Godin, B. Moss, A. Kafizas, S. Zafeiratos, J. R. Durrant, C. Petit, *Appl. Catal., B* **2019**, *242*, 369.
[28] A. Crake, K. C. Christoforidis, A. Gregg, B. Moss, A. Kafizas, C. Petit, *Small* **2019**, *15*, 1805473.
[29] A. Crake, K. C. Christoforidis, A. Kafizas, S. Zafeiratos, C. Petit, *Appl. Catal., B* **2017**, *210*, 131.
[30] A. L. da Silva, L. Wu, L. B. Caliman, R. H. R. Castro, A. Navrotsky, D. Gouvêa, *Phys. Chem. Chem. Phys.* **2020**, *22*, 15600.
[31] E. M. Dias, K. C. Christoforidis, L. Francàs, C. Petit, *ACS Appl. Energy Mater.* **2018**, *1*, 6524.
[32] M. Wang, D. Wang, Z. Li, *Appl. Catal., B* **2016**, *183*, 47.
[33] A. Kudo, A. Tanaka, K. Domen, T. Onishi, *J. Catal.* **1988**, *111*, 296.
[34] H. Lyu, T. Hisatomi, Y. Goto, M. Yoshida, T. Higashi, M. Katayama, T. Takata, T. Minegishi, H. Nishiyama, T. Yamada, Y. Sakata, K. Asakura, K. Domen, *Chem. Sci.* **2019**, *10*, 3196.
[35] H. Nishiyama, T. Yamada, M. Nakabayashi, Y. Maehara, M. Yamaguchi, Y. Kuromiya, Y. Nagatsuma, H. Tokudome, S. Akiyama, T. Watanabe, R. Narushima, S. Okunaka, N. Shibata, T. Takata, T. Hisatomi, K. Domen, *Nature* **2021**, *598*, 304.
[36] Q. Wang, J. Warnan, S. Rodríguez-Jiménez, J. J. Leung, S. Kalathil, V. Andrei, K. Domen, E. Reisner, *Nat. Energy* **2020**, *5*, 703.
[37] B. Moss, Q. Wang, K. T. Butler, R. Grau-Crespo, S. Selim, A. Regoutz, T. Hisatomi, R. Godin, D. J. Payne, A. Kafizas, K. Domen, L. Steier, J. R. Durrant, *Nat. Mater.* **2021**, *20*, 511.
[38] D. J. Kok, K. Irmscher, M. Naumann, C. Guguschev, Z. Galazka, R. Uecker, *Phys. Status Solidi A-Appl. Mater. Sci.* **2015**, *212*, 1880.
[39] Z. Su, F. Fang, X. Li, W. Han, X. Liu, K. Chang, *J. Colloid Interface Sci.* **2022**, *626*, 662.
[40] V. Mishra, M. K. Warshi, A. Sati, A. Kumar, V. Mishra, A. Sagdeo, R. Kumar, P. R. Sagdeo, *Mater. Sci. Semicond. Process.* **2018**, *86*, 151.
[41] M. Siebenhofer, A. Viernstein, M. Morgenbesser, J. Fleig, M. Kubicek, *Mater. Adv.* **2021**, *2*, 7583.
[42] S. Mochizuki, F. Fujishiro, S. Minami, *J. Phys.: Condens. Matter* **2005**, *17*, 923.
[43] A. Janotti, J. B. Varley, M. Choi, C. G. Van de Walle, *Phys. Rev. B* **2014**, *90*, 085202.
[44] R. A. De Souza, *Adv. Funct. Mater.* **2015**, *25*, 6326.
[45] M. L. Crespillo, J. T. Graham, F. Agulló-López, Y. Zhang, W. J. Weber, *Appl. Mater. Today* **2018**, *12*, 131.
[46] M. Abdi-Jalebi, Z. Andaji-Garmaroudi, S. Cacovich, C. Stavrakas, B. Philippe, J. M. Richter, M. Alsari, E. P. Booker, E. M. Hutter, A. J. Pearson, S. Lilliu, T. J. Savenije, H. Rensmo, G. Divitini, C. Ducati, R. H. Friend, S. D. Stranks, *Nature* **2018**, *555*, 497.
[47] S. Corby, L. Francàs, A. Kafizas, J. R. Durrant, *Chem. Sci.* **2020**, *11*, 2907.
[48] S. Corby, R. R. Rao, L. Steier, J. R. Durrant, *Nat. Rev. Mater.* **2021**, *6*, 1136.
[49] S. Selim, E. Pastor, M. Garcia-Tecedor, M. R. Morris, L. Francas, M. Sachs, B. Moss, S. Corby, C. A. Mesa, S. Gimenez, A. Kafizas, A. A. Bakulin, J. R. Durrant, *J. Am. Chem. Soc.* **2019**, *141*, 18791.
[50] L. Steier, I. Herraiz-Cardona, S. Gimenez, F. Fabregat-Santiago, J. Bisquert, S. D. Tilley, M. Gratzel, *Adv. Funct. Mater.* **2014**, *24*, 7681.
[51] Q. Wang, T. Hisatomi, M. Katayama, T. Takata, T. Minegishi, A. Kudo, T. Yamada, K. Domen, *Faraday Discuss.* **2017**, *197*, 491.
[52] P. Giannozzi, S. Baroni, N. Bonini, M. Calandra, R. Car, C. Cavazzoni, D. Ceresoli, G. L. Chiarotti, M. Cococcioni, I. Dabo, A. Dal Corso, S. de Gironcoli, S. Fabris, G. Fratesi, R. Gebauer, U. Gerstmann, C. Gougoussis, A. Kokalj, M. Lazzeri, L. Martin-Samos, N. Marzari, F. Mauri, R. Mazzarello, S. Paolini, A. Pasquarello, L. Paulatto, C. Sbraccia, S. Scandolo, G. Sclauzero, A. P. Seitsonen, et al., *J. Phys.-Condens. Matter* **2009**, *21*, 395502.
[53] S. Scandolo, P. Giannozzi, C. Cavazzoni, S. d. Gironcoli, A. Pasquarello, S. Baroni, *Z.r Kristallogr. – Cryst. Mater.* **2005**, *220*, 574.
[54] D. Vanderbilt, *Phys. Rev. B* **1990**, *41*, 7892.
[55] J. P. Perdew, K. Burke, M. Ernzerhof, *Phys. Rev. Lett.* **1996**, *77*, 3865.
[56] V. I. Anisimov, M. A. Korotin, A. S. Mylnikova, A. V. Kozhevnikov, D. M. Korotin, J. Lorenzana, *Phys. Rev. B* **2004**, *70*, 172501.
[57] M. Cococcioni, S. de Gironcoli, *Phys. Rev. B* **2005**, *71*, 035105.
[58] S. L. Dudarev, G. A. Botton, S. Y. Savrasov, C. J. Humphreys, A. P. Sutton, *Phys. Rev. B* **1998**, *57*, 1505.
[59] M. Farnesi Camellone, P. M. Kowalski, D. Marx, *Phys. Rev. B* **2011**, *84*, 035413.
[60] B. J. Morgan, G. W. Watson, *Surf. Sci.* **2007**, *601*, 5034.
[61] S. Grimme, J. Antony, S. Ehrlich, H. Krieg, *J. Chem. Phys.* **2010**, *132*, 154104.
[62] N. Marzari, D. Vanderbilt, A. De Vita, M. C. Payne, *Phys. Rev. Lett.* **1999**, *82*, 3296.
[63] N. Seriani, C. Pinilla, Y. Crespo, *J. Phys. Chem. C* **2015**, *119*, 6696.